Opto-Electronic Advances

CN 51–1781/TN ISSN 2096–4579 (Print) ISSN 2097–3993 (Online)

Ultra-high-*Q* photonic crystal nanobeam cavity for etchless lithium niobate on insulator (LNOI) platform

Zhi Jiang, Cizhe Fang, Xu Ran, Yu Gao, Ruiqing Wang, Jianguo Wang, Danyang Yao, Xuetao Gan, Yan Liu, Yue Hao and Genquan Han

Citation: Jiang Z, Fang CZ, Ran X, et al. Ultra-high-Q photonic crystal nanobeam cavity for etchless lithium niobate on insulator (LNOI) platform. *Opto-Electron Adv* **8**, 240114(2025).

https://doi.org/10.29026/oea.2025.240114

Received: 16 May 2024; Accepted: 19 August 2024; Published online: 31 October 2024

Opto-Electronic Advances

Article

January 2025, Vol. 8, No. 1

DOI: 10.29026/oea.2025.240114 CSTR: 32247.14.oea.2025.240114

Ultra-high-*Q* photonic crystal nanobeam cavity for etchless lithium niobate on insulator (LNOI) platform

Zhi Jiang[1], Cizhe Fang[1,3], Xu Ran[1], Yu Gao[1], Ruiqing Wang[1], Jianguo Wang[2], Danyang Yao[1]*, Xuetao Gan[2]*, Yan Liu[1,3], Yue Hao[1] and Genquan Han[1,3]

The expansive spectral coverage and superior optical properties of lithium niobate (LN) offer a comprehensive suite of tools for exploring novel functionalities. Achieving high-quality (*Q*) photonic resonator cavities is crucial for enhancing light-matter interactions. However, this task is challenging as the device performance is heavily dependent on the fabrication quality of the LN. In this paper, we present experimental validation of an etchless approach to fabricating high-*Q* photonic crystal nanobeam cavities (PCNBCs). We successfully fabricate PCNBCs with *Q* factors exceeding 10^5 while maintaining high transmittance by capitalizing on the low waveguide loss and high fabrication tolerance of TE-polarized mode. Remarkably, the *Q* factor achieved here exceeds previous reports on etchless LN PCNBCs by over an order of magnitude. Benefiting from this advancement, we further explore a variety of optical functions, including thermo-optic tuning, optically induced bistability, and Fano line shapes generation. These findings present promising prospects for a versatile platform technique, facilitating the development of high-performance electro-optic or acousto-optic modulators, optical logic devices, and quantum photonics, highlighting its significant impact in the field of photonic integration.

Keywords: photonic crystal nanobeam cavity; LNOI platform; high *Q*; thermo-optic tuning; bistability; Fano line shapes

Jiang Z, Fang CZ, Ran X et al. Ultra-high-*Q* photonic crystal nanobeam cavity for etchless lithium niobate on insulator (LNOI) platform. *Opto-Electron Adv* **8**, 240114 (2025).

Introduction

The interaction between light and matter establishes the first basis for essential components that enable on-chip photon manipulation technologies[1]. Conventional silicon-based photonic crystal nanobeam cavities (PCNBCs) strongly confine light with both high-quality (*Q*) factors and small mode volumes, dramatically enhancing these interactions[2]. Additionally, these cavities can further synergize with the thermo-optic (TO)[3] or free-carrier dispersion (FCD) effect[4], enabling a broad spectrum of applications across multiple disciplines. Notable examples include high-efficiency optical modulators and switches[5,6], ultra-compact filters[7], and advanced nonlinear optics[8]. However, the modulation speed of silicon

[1]State Key Laboratory of Wide-Bandgap Semiconductor Devices and Integrated Technology, School of Microelectronics, Xidian University, Xi'an 710071, China; [2]Key Laboratory of Light Field Manipulation and Information Acquisition, Ministry of Industry and Information Technology, and Shaanxi Key Laboratory of Optical Information Technology, School of Physical Science and Technology, Northwestern Polytechnical University, Xi'an 710129, China; [3]Hangzhou Institute of Technology, Xidian University, Hangzhou 311200, China.

*Correspondence: DY Yao, E-mail: dyyao@xidian.edu.cn; XT Gan, E-mail: xuetaogan@nwpu.edu.cn

Received: 16 May 2024; Accepted: 19 August 2024; Published online: 31 October 2024

photonics is primarily constrained by its inherent absorptive and nonlinear characteristics, which has led to a plateau in its development, making it challenging to satisfy the exponentially increasing demand for large-capacity interconnects and communications[9]. On the other hand, lithium niobate ($LiNbO_3$, LN), although an "old" and extensively studied material, has played a crucial role in advancing photonics and acoustics for several decades[10]. From enabling high-speed optical communications[11] to the development of acoustic filters used in mobile terminals[12], LN has proven its versatility and reliability. Specifically, in photonics, its extraordinarily strong and highly linear electro-optic (Pockels) properties have propelled LN optical modulators into the Terabit era[13].

Inheriting the exceptional optical properties of LN, thin-film lithium niobate on insulator (LNOI) has recently been recognized as a cutting-edge platform that is leading another revolution in integrated photonics on chip[14–16]. Contrasting with the CMOS-compatible process of silicon photonics, LNOI photonics encounters a significant barrier in manufacturing low-loss waveguides and nanoscale optical components[10]. The principal challenge is the high-quality etching of LN. While precise methods like ion beam etching[17] and focused ion beam (FIB) milling[18] are accurate, they can damage the crystal lattice and introduce ion contamination. An alternative technique, the femtosecond laser photolithography assisted chemo-mechanical etching (PLACE) technique[19–21], overcomes these issues and ensures an ultrasmooth surface but lacks sufficient etching selectivity for fabricating sophisticated structures such as PCNBC. Moreover, methods such as reactive ion etching (RIE) and inductively coupled plasma etching (ICP-RIE), while compatible with batch fabrication, suffer from significant redeposition issues[10]. These challenges collectively hinder the enhancement of optical performance in LN-based devices.

Recently, a novel route has been proposed that involves spinning and patterning a low-refractive-index polymer (~1.5) on top of the LNOI substrate[22]. This approach allows for the creation of a polymer-loaded rib-waveguide capable of accommodating both transverse electric (TE) and transverse magnetic (TM) modes. Nonetheless, most research efforts have primarily focused on TM-polarized modes produced by photonic bound states in the continuum (BIC)[23]. On this etchless platform, various intriguing physical phenomena[24,25] and high-performance key optical components have been demonstrated[26–28]. In addition, many other novel applications have also been unlocked in the metasurfaces based on the BIC regime[29,30]. However, there are challenges when it comes to manufacturing high-Q resonator cavity devices due to the highly sensitive radiation losses of the TM mode associated with the polymer stripe widths. In comparison, the TE modes represent standard bound modes that propagate without radiation losses for any width within their supported range[31]. Therefore, the design strategy for the polymer/LN hybrid structure still has room to be developed.

In this paper, we present an experimental demonstration highlighting the significant potential of TE-polarized polymer-loaded waveguides as a feasible pathway for the realization of highly efficient and productive nanocavities. To the best of our knowledge, the achieved Q factor is over one order of magnitude higher than any previously reported etchless LN PCNBCs (~0.1×10^5)[26,32]. This remarkable enhancement in Q inspire a series of strong light-matter interaction phenomena, including highly efficient thermo-optic (TO) tuning, exceptionally strong optical bistability, and facile generation of Fano resonances. Our successful demonstration of high-Q LNOI photonic cavities represent a significant milestone towards the development of LN nanophotonics, merging the unique material properties of LN with versatile nanophotonic device design and fabrication methods. This breakthrough holds tremendous promise for a wide range of applications, including nonlinear photonics, electro-optic (EO) or acousto-optic (AO) tunable devices, optical logic devices, and quantum photonics.

Methods

Device design

Figure 1(a) depicts the cross-section view of the polymer-loaded waveguide, which is placed on a y-cut LNOI substrate. The loaded polymer has a thickness of 0.4 μm and a width of w. To obtain the optimal w, the finite element method (FEM) is employed to model the propagation loss of this waveguide. In our simulations, the refractive index of the polymer is set to 1.53, and the refractive index of ordinary (n_o) and extraordinary (n_e) for LN are 2.21 and 2.14, respectively. Figure 1(b) illustrates the relationship between the propagation loss and waveguide width w for different modes at the wavelength of 1550 nm. It is observed that TM modes exhibit minimal losses

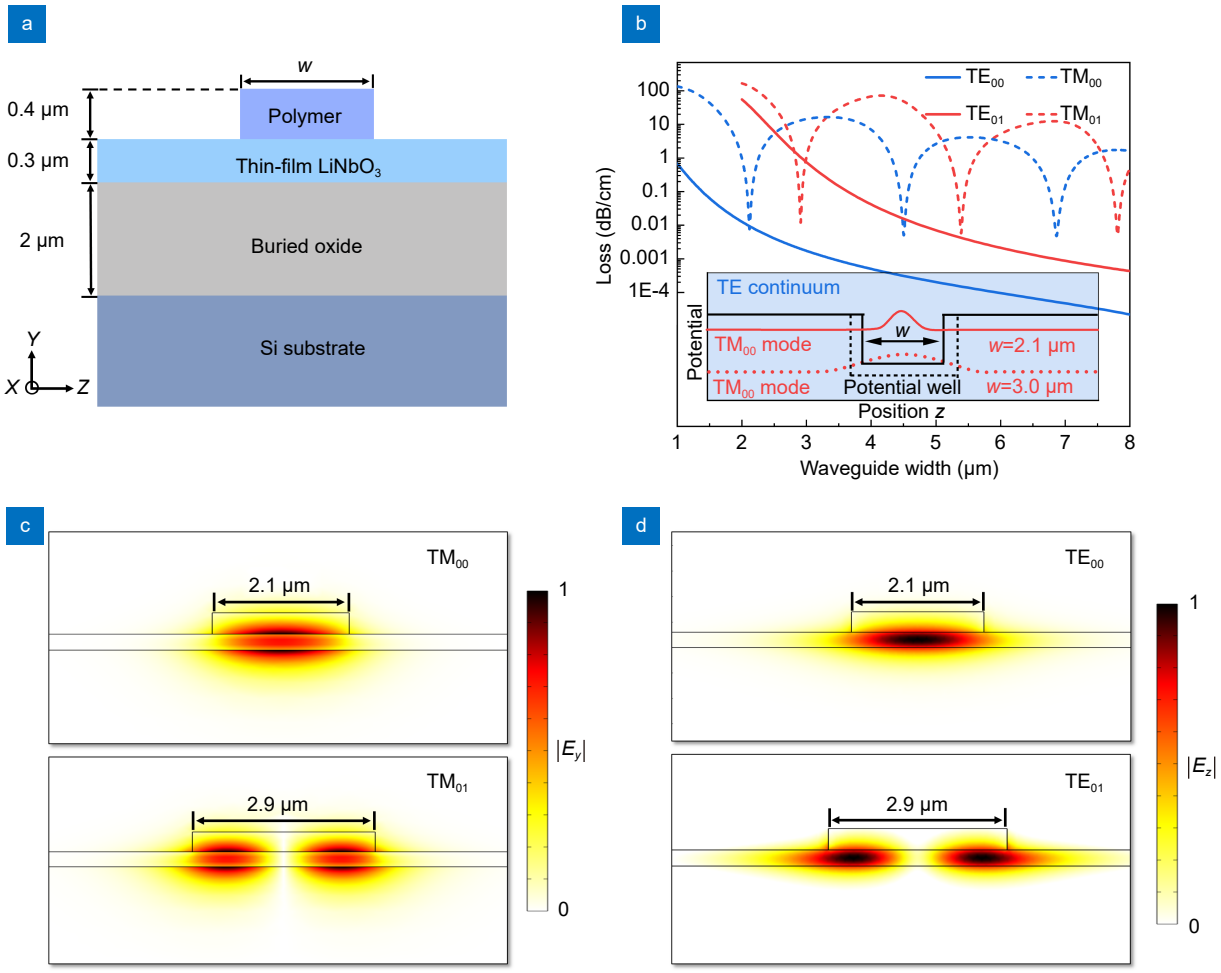

Fig. 1 | (**a**) The schematic of the polymer-loaded waveguide. (**b**) The waveguide loss of different optical modes vs. waveguide width *w* at 1550 nm. The inset illustrates the photonic potential distribution for the TM_{00} mode at various waveguide widths. The blue background represents the TE continuum. (**c**) The electric field ($|E_y|$) profiles for TM_{00} and TM_{01} modes. (**d**) The electric field ($|E_z|$) profiles for TE_{00} and TE_{01} modes.

at certain specific waveguide widths. This behavior can be explained from the perspective of the photon potential[23], as shown in the inset of Fig. 1(b). The energy of the TM mode can couple into the TE continuum through the edges of the waveguide due to the potential well of the TM mode being located within the TE continuum. By adjusting *w*, it is possible to eliminate coupling loss through destructive interference between the coupling channels. In this mechanism, the TM mode exhibits lower loss at *w* of 2.1 μm compared to 3.0 μm, due to stronger confinement within the potential well. By contrast, for TE modes, the potential well has the lowest energy and is not coupled with TE continuum in the LN substrate (not shown). Therefore, the propagation loss of TE modes is low and stable, decreasing as *w* increases. Consequently, TE modes are robust compared to TM modes, a characteristic of critical importance given that fabrication tolerances have a lesser impact on device performance.

To reveal the light propagation mechanism within the waveguide, an analysis of optical modes with electric field profiles was performed. Figure 1(c) displays the electric field profiles of $|E_y|$ for both TM_{00} and TM_{01} modes, revealing energy concentrated in the upper and lower cladding layers. Correspondingly, Fig. 1(d) illustrates electric field profiles of $|E_z|$ for both TE_{00} and TE_{01} modes, confirming the predominant localization within the LN layer, which facilitates the effective utilization of the outstanding material properties. Compared to the TM modes, the TE modes exhibit relatively weaker confinement in the *z*-direction, potentially resulting in larger losses in designs involving curved waveguides. Nevertheless, the transmission characteristics of the TE modes are instrumental in avoiding the disruption of BIC condition caused by the anisotropy of LN. This feature is very important for the design of high-*Q* PCNBC.

Based on the discussion of waveguide modes and

optical losses above, we further investigate the losses inside the nanocavity. As illustrated in Fig. 2(a), the proposed PCNBC is constructed by a series of dielectric blocks in two regions, including taper and mirror, which are symmetrical with the red dashed line. The width of the polymer waveguide is 2 μm, and the fixed lattice constant of a = 0.43 μm enables phase matching for each unit cell. In the taper region, pulling the confined mode with a Gaussian-shaped field profile away from the light line effectively minimizes radiation loss[33]. It is realized by establishing a parabolic distribution of the filling factor[34], which is utilized to define the dimension of the dielectric block. Here, the filling factor f is defined as the ratio of the air area to that of the unit cell. The relationship of the filling factor from the center of PCNBC (f_c) to the end of the taper region (f_e) is

$$f_i = f_c - (f_c - f_e)i^2/N_t^2 , \quad (1)$$

where N_t represents the number of dielectric blocks in the taper region, and i is an integer increasing from 0 to N_t. f_c and f_e are determined by mirror strength γ, which is determined by[34]

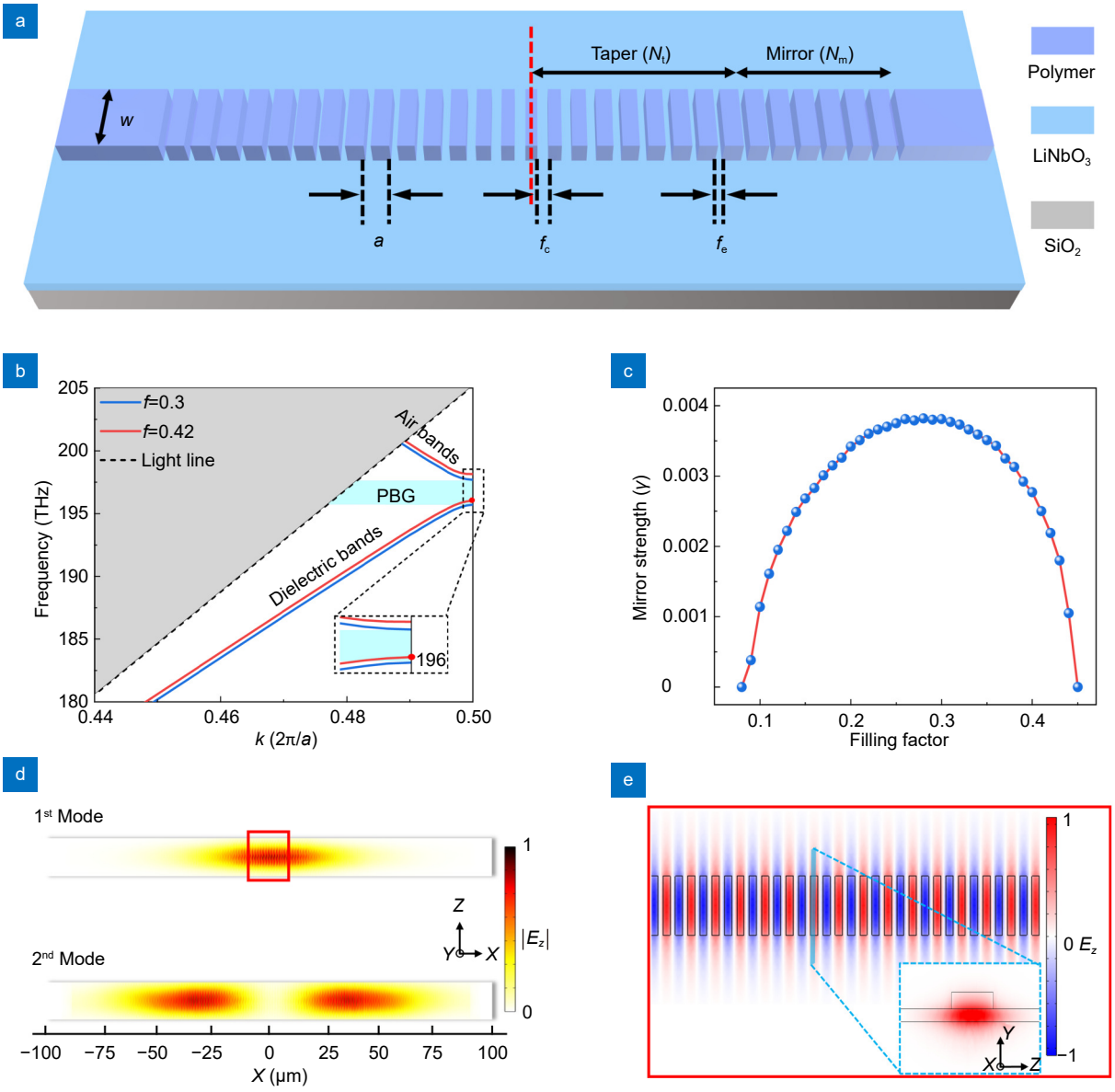

Fig. 2 | (**a**) Schematic diagram of the polymer-loaded PCNBC. (**b**) The band diagram of the TE_{00} modes for different filling factors: f = 0.3 (blue line) and f = 0.42 (red line). The inset shows the enlarged boxed region and the resonant frequency of the fundamental mode is marked with a red dot. (**c**) The mirror strength vs. filling factor. (**d**) The top views of the electric field ($|E_z|$) profile for the fundamental mode and second-order mode. The orientation of the PCNBC is along the x direction of the LN crystal. (**e**) Electric field (E_z) distribution profile of the magnified region in (d). The inset shows the electric profile at the y-z plane.

$$\gamma = \sqrt{(\omega_0 - \omega_1)^2/(\omega_0 + \omega_1)^2 - (\omega_{res} - \omega_2)^2/\omega_2^2}\,, \quad (2)$$

where ω_{res} is the target resonance frequency of the fundamental mode, and ω_0, ω_1, ω_2 are the air band edge, dielectric band edge, and midgap frequency of each segment. Figure 2(b) shows the band diagram of the TE_{00} mode. The filling factors of 0.3 and 0.42 are chosen, which correspond to the maximum mirror strength and the minimum mirror strength (see Fig. 2(c)). As shown in Fig. 2(b), a photonic band gap (PBG) is obtained at f = 0.3 (blue curves). When f is 0.42 (red curves), the dielectric band is pulled into the PBG. It means that the fundamental mode becomes a discrete mode. As a result, f_c is set to 0.42 and f_e to 0.3. The filling factor is gradually changing from f = 0.3 to f = 0.42 according to Eq. (1). At the mirror region, the filling factor remains the same (i.e., f_e = 0.3).

Next, we investigate the optical mode field profile of the PCNBC based on the above parameters. To better confine optical mode, the transition from f_e to f_c should be smoother. Thus, the numbers of N_t and N_m are set to N_t = 120 and N_m = 100, respectively. Figure 2(d) illustrates the simulation results for the profile of Gaussian-shaped electric field energy for the fundamental and second-order modes. It indicates that the PCNBC we designed has the capability to support other high-order resonant modes. Furthermore, as depicted in Fig. 2(e), the electric field distribution of the fundamental mode is parallel to the z-axis of the LN crystal. Thus, it confirms the optical mode of the PCNBC is based on TE_{00} mode. The relationship between w, N_t, N_m, and Q will be discussed in detail in the next section.

Device fabrication

Devices were fabricated on a custom-made y-cut LNOI substrate with a 0.3 μm LN layer (NanoLN Corp.). The substrate is cleaned sequentially in N-methyl-2-pyrrolidone (90 °C), isopropyl alcohol (ultrasonic), deionized water (ultrasonic), and piranha solution (90 °C) for 10 minutes, respectively. Then a 0.4 μm polymer (ARP-6200.13) was spin-coated on the substrate and prebaked on a hot plate at 180 °C for 10 minutes. The pattern was transferred to the polymer by e-beam lithography (NanoBeam, nB5). Finally, the residual polymer was removed with the developer. Figure 3(a) shows the scanning electron microscope (SEM) image of the sample. The polymer waveguide is well-defined, which guarantees its process stability.

Device characterization

To characterize the proposed device, the light from the tunable semiconductor laser (Santec, TSL-550) is pumped into the grating coupler through a polarization controller, which is used to adjust the polarization of the pump light. The transmitted light of PCNBC is collected by the optical power meter (Thorlabs, PM100D) from the other grating coupler. Throughout the testing process, the chip is placed on a high-accuracy thermoelectric cooler (TEC) with a stabilized temperature of 21.5 °C. As shown in Fig. 3(b), there exist several peaks. The fundamental mode is located at 1528.320 nm, which is close to the simulated result of 1530.612 nm (the fundamental mode resonance wavelength in Fig. 2(d)). The slight deviation can be attributed to the influence of the fabrication. Other high-order modes appear at larger wavelengths. Compared with the high-order modes, the fundamental mode has a higher Q factor of 0.47×10^5 (see the inset in Fig. 3(b)) and a lower transmission of 52.4%. Since only the fundamental mode is optimized, the high-order modes suffer a larger radiation loss. Moreover, the coupling loss quality factor (Q_c) from the PCNBC to the bus waveguide and the radiation loss quality factor (Q_r) can be used to determine transmission (T)[35]

$$T = Q_r^2/(Q_c + Q_r)^2\,. \quad (3)$$

For radiation-Q-limited PCNBC, Q_c is much larger than Q_r. According to Eq. (3), the high-order modes exhibit larger transmissions due to their smaller values of Q_c. Figure. 3(c) describes the relationship between the Q factor of the fundamental mode and w (N_t = 120, N_m = 100, f_c = 0.42, and f_e = 0.3). The Q factor becomes larger along with w because a larger w results in a smaller propagation loss (see Fig. 1(b)).

Here, we discuss the influence of the dielectric block on the Q factor. Figure 3(d) presents the transmission spectrum at different N_t, revealing that as N_t increases, the Q factor correspondingly rises, while the transmission gradually diminishes. A similar behavior is observed in Fig. 3(e) for varying values of N_m. These results can be attributed to three mechanisms. First, an increased number of dielectric blocks in the taper region leads to a more gradual parabolic distribution of the filling factor, ranging from 0.3 to 0.42. This design facilitates a more uniform confinement of the optical Gaussian-shaped field profile along the x-direction, thereby minimizing the scattering of optical energy into radiation modes. Second, a higher value of N_m enhances the

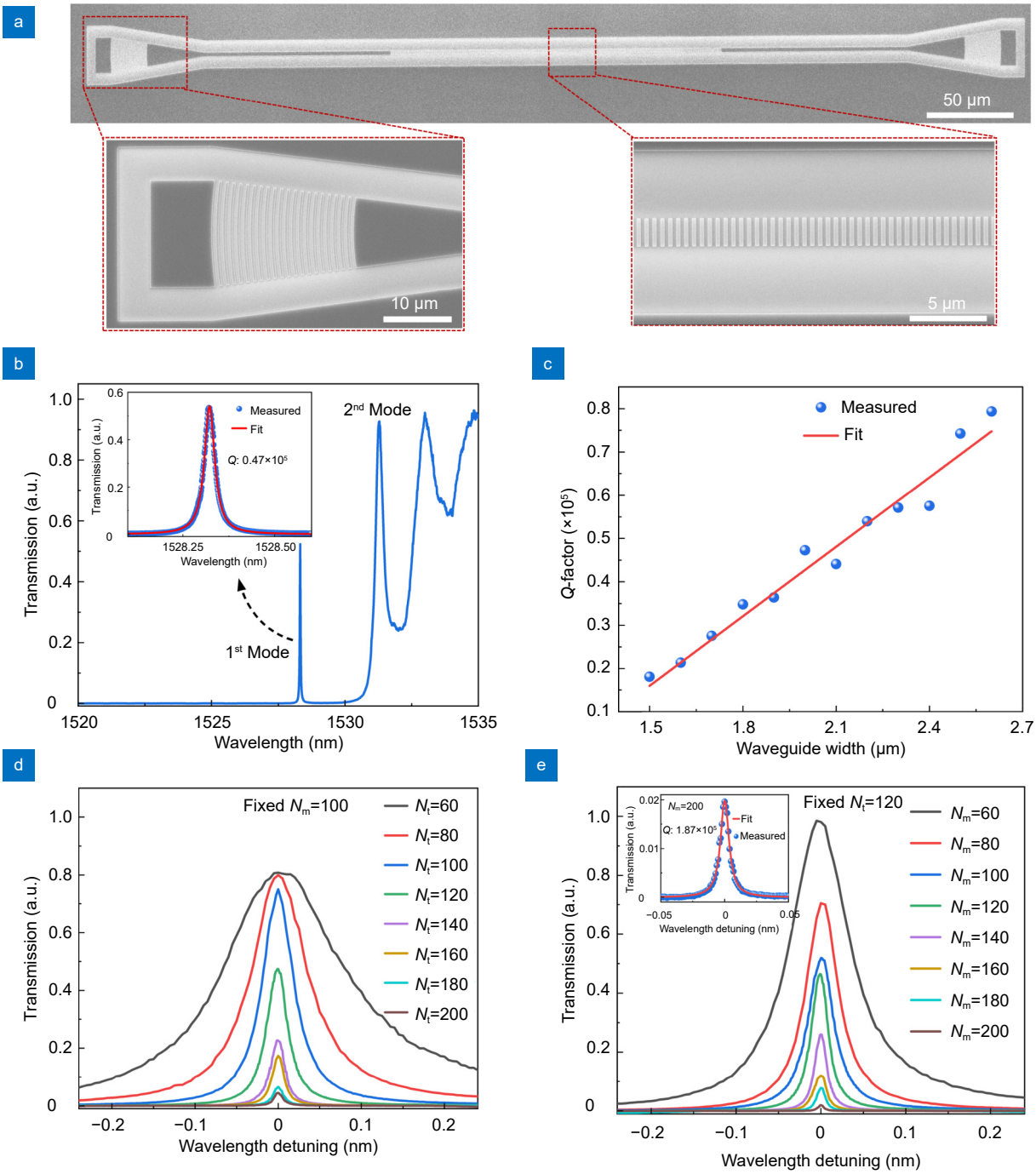

Fig. 3 | (**a**) SEM image of the fabricated PCNBC. The bottom insets show the grating coupler (left) and the central region of the cavity (right), respectively. (**b**) Measured transmission spectrum of a cavity with f_c = 0.42, f_e = 0.3, N_t = 120, N_m = 100, and w = 2 μm. Inset: the detailed transmission spectrum of the fundamental mode is fitted with a Lorentzian line shape at around 1528.320 nm. (**c**) Measured Q factors of the fundamental mode vs. waveguide width w. (**d**) Measured transmission spectra of the fundamental mode for different N_t at N_m = 100. (**e**) Measured transmission spectra of the fundamental mode for different N_m at N_t = 120. The inset shows the Lorentzian fitting of the transmission spectrum at N_m = 200.

mirror reflectivity, which significantly strengthens the confinement of the Gaussian-shaped field profile within the PCNBC. Third, an increase in both N_t and N_m can reduce the coupling losses, which result in reduced transmission, as illustrated in Eq. (3). Combining these mechanisms, the increasing Q factors with the number of dielectric blocks can be attributed to a tighter Gaussian-shaped field profile, resulting in reduced cavity losses and coupling losses. Thereby, the properly optimal N_m and N_t parameters are crucial for achieving high-Q and

high-transmission PCNBCs that are much more desirable for high-efficient optical modulators. Despite a decrease in transmission, the Q increases to above 1.87×10^5 when N_m is set to 200, as shown in the inset of Fig. 3(e). Table 1 presents a comparison of the reported LN-based PCNBCs. Noted that, our PCNBCs exceed the most similar cavities on LN substrate, featuring a much simpler fabrication process[36].

Discussion on *Q*-induced optical phenomena

The high Q factor of PCNBCs enhance the light-matter interactions, enabling the exploration of intriguing novel optical phenomena. In this section, the potential functions of the Q-induced phenomen based on our LN PCNBCs are examined and studied.

Thermo-optic tuning

TO tuning is one of the most efficient methods to manipulate photons, providing a significant refractive index change almost without optical loss[40,41]. This mechanism plays a crucial role in photonic integrated circuits (PICs), where TO switches and modulators are indispensable components[42,43]. For example, optical devices like microring resonators and PCNBCs, are highly sensitive to fabrication errors leading to resonance wavelength shifts. This problem can be solved by integrating a heater near the waveguide. The optical material with a large TO coefficient is critical for achieving highly energy-efficient TO tuning. Nevertheless, in the proposed LNOI platform, the maximum TO coefficient of the LN is $\mathrm{d}n_e/\mathrm{d}T \approx 3.3\times10^{-5}\ \mathrm{K}^{-1}$, which is smaller than that of the polymer material as reported[44]. For our PCNBCs, polymer serves not only as the structural element but also facilitates TO tuning compared to monolithic LN, since part of the optical mode is distributed within the polymer layer. The TO tuning capability of polymers has been demonstrated in various types of PCNBCs[45,46]. Generally, to evaluate the modulation efficiency of the TO modulator, the π-phase shift temperature ΔT_π is calculated by[47]

$$\Delta T_\pi = \pi\delta\lambda_0(\Delta\lambda/\Delta T)^{-1}\,, \tag{4}$$

where $\delta\lambda_0$ is the linewidth, corresponding to the full width at half maximum (FWHM) of the transmission spectrum, and $\Delta\lambda/\Delta T$ is the sensitivity of temperature, which is determined by the material properties. To improve modulation efficiency, it often involves complex structures and fabrication processes, such as suspended device structures and p-n junction waveguides[48,49]. High modulation efficiency and a simple fabrication process are desirable for TO tuning, especially in LN photonics with a weak TO coefficient.

To study the thermal tuning characteristics of our PCNBCs, the chip is heated from 20 °C to 30 °C at a step of 2 °C. The transmission spectra for a PCNBC operating in the fundamental mode are presented in Fig. 4(a). The resonance peak redshifts obviously as the temperature rises and ΔT_π of 2.36 °C is obtained. Therefore, the device possesses TO tuning capability. In general, an increase in the Q tends to reduce the ΔT_π of the TO modulator, as shown in Eq. (4), indicating a lower power consumption. For this purpose, devices with different Q factors are measured under the same condition. The corresponding ΔT_π and $\Delta\lambda/\Delta T$ are shown in Fig. 4(b). With the increase in the Q factor, the ΔT_π reduces. It is due to a larger optical energy density that enhances light-matter interactions. A device with a larger Q is suitable for temperature-sensitivity applications. The sensitivity of temperature remains around 26 pm/°C as the Q increases, which reveals the $\Delta\lambda/\Delta T$ of this platform. ΔT_π reaches

Table 1 | Comparison of various PCNBCs on LN substrate.

Device structure	Polarization modes	Q ($\times10^5$)	Transmission (%)	Extinction ratio (dB)	Footprint (μm²)
Si_3N_4 PCNBC/LNOI[37]	TE	0.09	-	32	1.6×140
LN PCNBC/Suspend[38]	TE	1.09	24	-	0.75×37
Si PCNBC/LN[39]	TE	1.2	1.6	-	1.8×35.5
LN PCNBC/LNOI[36]	TE	1.34	-	11.5	1.2×30
Polymer PCNBC/LNOI[32]	TM	0.07	38	-	1.8×118
Polymer PCNBC/LNOI[26]	TM	0.12	15	-	2.1×122
Polymer PCNBC/LNOI[this work, A]	TE	1.04	16.6	25	2×189
Polymer PCNBC/LNOI[this work, B]	TE	1.87	2	22	2×223

Dimensions of A: w = 2 μm, N_t = 120, N_m = 140, f_c =0.42, and f_e = 0.3.

Dimensions of B: w = 2 μm, N_t = 120, N_m = 200, f_c =0.42, and f_e = 0.3.

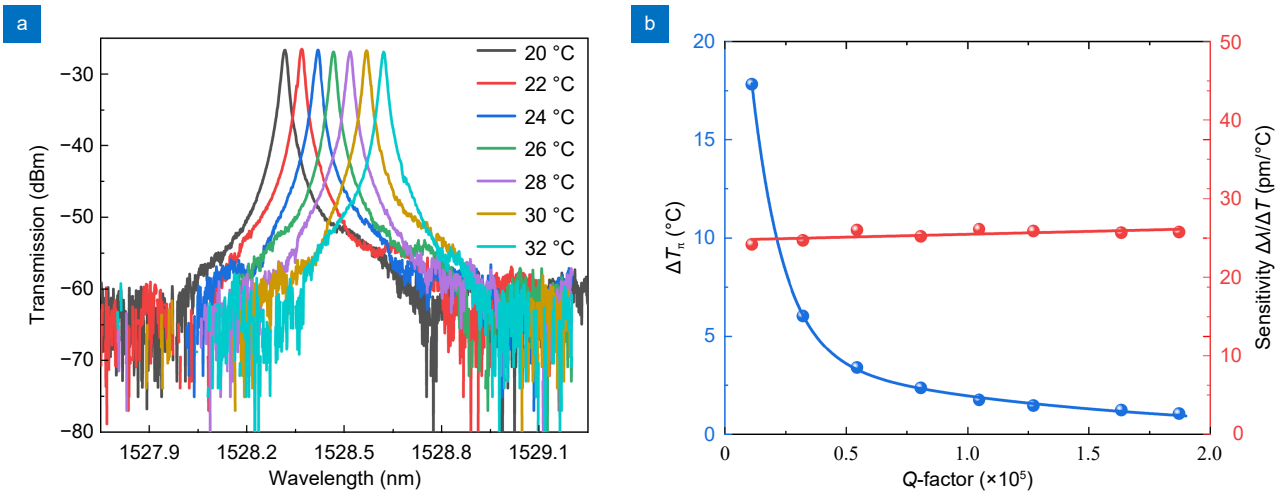

Fig. 4 | (**a**) Measured transmission spectra of the PCNBC at different temperatures. The *Q* factor of the PCNBC is 0.8×10⁵. (**b**) Measured ΔT_π and the sensitivity of temperature for various devices with different *Q* factors.

its minimum value of 1.05 °C when the *Q* reaches 1.87×10⁵, surpassing the performance of a device employing TO tuning with an integrated metal heater[7,45]. Through the measured data and the results from FEM calculations, the TO coefficient of the polymer is extracted as 0.8×10^{-4} K^{-1}. Most importantly, the demonstration of thermal tuning indicates that the proposed high-*Q* PCNBCs provide a novel solution to the TO tuning issues experienced by LN photonics while also allowing for easy fabrication processes.

Optical bistability

Optical bistability is a phenomenon observed in high-*Q* silicon photonics, predominantly attributed to complex nonlinear effects such as two-photon absorption (TPA), the TO effect, FCD, and the Kerr effect[50]. This bistability is critical for the development of next-generation all-optical applications, including high-speed modulation and optical logic circuits[51,52]. LN, despite its widespread use in photonic applications, has a poor TO coefficient and lacks a mechanism for TPA at 1550 nm due to its wide bandgap of 3.78 eV[53]. Therefore, it is nontrivial to excite optical bistability even in microcavities, limiting its potential for all-optical modulation. In contrast, the polymer introduces inherent defect absorption and has a large TO coefficient as previously discussed in TO tuning. Moreover, the high-*Q* PCNBC may facilitate this process due to the small mode volume and strong confinement of the Gaussian-shaped field profile. Taking into account the above-mentioned analysis, it is a feasible solution to facilitate the application of LN photonics in all-optical information processing. Consequently, we investigate optically-induced bistability in the proposed high-*Q* PCNBCs.

First, we set the tunable semiconductor laser with wavelength increment steps of 1 pm, and the required sample time is 0.37 seconds for each point. Second, we measure the transmission spectrum for the fundamental mode at different input power levels. At this state, the power-dependent transmission spectra for one of the PCNBCs are shown in Fig. 5(a). As the power injected into the cavity increases from 72.4 μW to 738.9 μW, there are two significant changes are observed. The resonance peak exhibits a pronounced redshift, which is induced by the positive TO coefficient of LN and polymer. Additionally, the measured line shapes gradually change from a Lorentzian type to a bistability feature induced by the TO effect. The optical bistability comes into being when the shift ($\Delta\lambda$) of the transmission spectrum satisfies the Eq. (5)[54]. Meanwhile, Eq. (5) indicates that a PCNBC with a large *Q* factor (small linewidth) will benefit under the identical condition, which requires lower optical power to induce bistability. The corresponding injected power is defined as the threshold power P_t. For this device, P_t is 160 μW.

$$\Delta\lambda \geqslant \sqrt{3}\delta\lambda_0/2\,. \tag{5}$$

Figure 5(b) illustrates the threshold power of optical bistability for different devices with varying *Q* factors and transmissions. Initially, the threshold power gradually decreases as the *Q* increases, which agrees with our prediction. The underlying mechanism is mainly due to the dramatically enhanced optical energy density in PC-

NBC. When the Q exceeds 1.63×10^5, the threshold power begins to increase. It is caused by the decline in transmission intensity with increasing Q. Therefore, achieving high-efficient optical bistability depends on the careful design of PCNBCs with both high Q factors and optimal transmission characteristics. This experiment validates the feasibility of LN photonics devices with optical response, potentially paving the way for the development of LN all-optical logic chips.

Fano resonance

Fano resonance, characterized by its sharp and asymmetric line shape, opens up extensive prospects for the advancement of the field of photonics, especially proving immensely attractive in the realms of switching and sensing[55,56]. Numerous efforts have been put to demonstrate high-performance Fano resonance[57,58]. However, these devices often suffer from a larger footprint and complex tunability. Recently, the tunable Fano line shapes have been demonstrated in the silicon-based 1D PCNBC by adjusting the position of the input and output fibers[59]. This efficient Fano tunability benefits from two aspects. First, the high-index-contrast silicon waveguide ensures strong confinement of light within the waveguide. Second, the rectangular photonic crystal grating couplers provide heightened light sensitivity. All these factors enhance the dependency of the grating on the position of the fiber. However, achieving highly efficient Fano tunability on this etchless LNOI platform remains challenging due to the wake interaction between discrete state (cavity resonance mode) and continuum state (waveguide propagating mode). Therefore, the high-Q PCNBCs provide a good platform for studying the high-efficiency generation of Fano resonance.

When the pump laser is near the resonance wavelength of the PCNBC, part of the energy is converted into the high-order leak TE mode, which serves as a continuous state and can propagate through the PCNBC[59,60]. Then, it interferes with the discrete fundamental mode. The transmission spectrum produced by the interaction is described as follows[61]

$$|T(\omega)|^2 = T_0 + k\frac{[q+2(\omega-w_0)/\Gamma]^2}{1+[2(\omega-w_0)/\Gamma]^2}\,, \tag{6}$$

$$q = \cot\varphi\,, \tag{7}$$

where T_0 and k are the constant factors of offset and scaling factor. And q, φ, w_0, and Γ are the Fano asymmetry factor, the phase difference between the continuum state and discrete state, the resonance frequency of the cavity mode, and the resonance linewidth, respectively.

To introduce the interference, the positions of the input fiber (left red dot) and output fiber (right red dot), located at the top of the grating couplers, are gradually altered, as illustrated in Fig. 6(a). When two fibers perfectly coincide with the center of the grating couplers, the phase difference φ between the continuum state and the discrete fundamental mode is zero, and the measured transmission spectrum has a Lorentzian line shape. However, the phase difference φ is not zero when the fibers are off-center from the grating couplers, the two

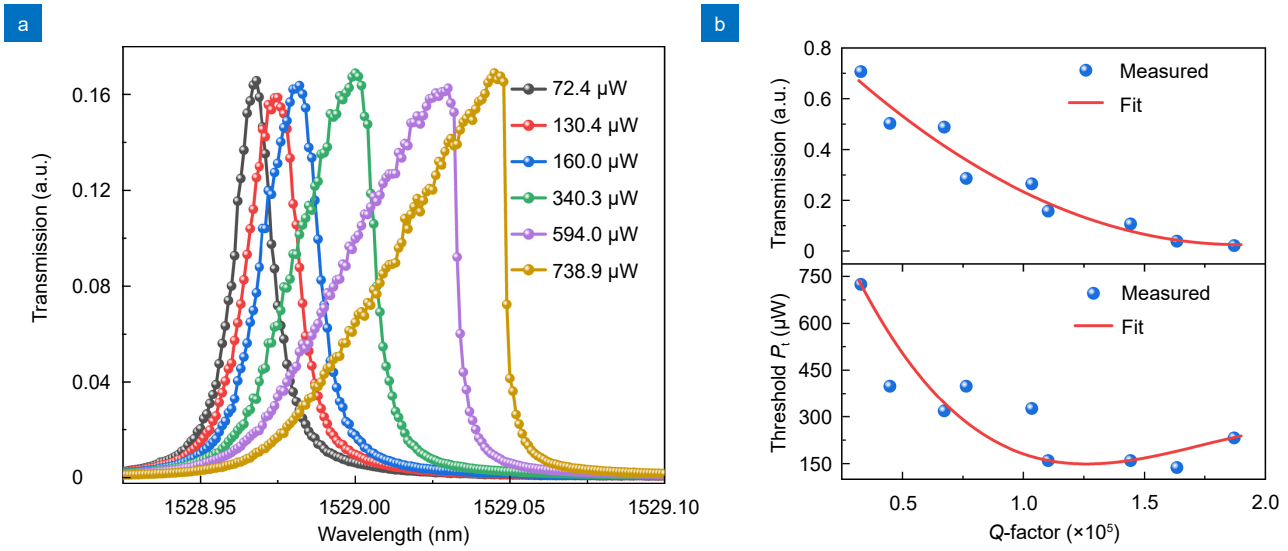

Fig. 5 | (**a**) The measured transmission spectra of a PCNBC (Q is 1.04×10^5) at different input powers. The threshold power is 160 μW. (**b**) The measured threshold power for the devices with different transmissions and Q factors.

modes start to interfere with each other, and the measured transmission spectrum has an asymmetric Fano line shape. In this approach, the transmission spectrum will experience a π phase shift change in theory. That is, the transmission spectrum will go through Lorentzian, Fano, quasi-Lorentzian, inverted Fano, and Lorentzian line shapes[62].

The measured transmission spectra are displayed in Fig. 6(b). For simplification and effective monitoring of the interference, the output fiber is fixed at y_o = 3 μm. To change the phase, the input fiber is moved from y_i = 2 μm to y_i = 6 μm in the direction of y_i at a step of 2 μm. During this process, the measured transmission spectra show a significant change. With the increase in y_i, the extinction ratio (ER) reaches 15.14 dB, 19.03 dB, and 25.43 dB for the φ values of 0.24 rad, 0.43 rad, and 0.58 rad. When the input fiber goes along $-y_i$ with the same displacement, the inverted Fano line shapes are obtained. The corresponding ER is 25.83 dB, 16.38 dB, and 12.89 dB, with φ being −0.09 rad, −0.19 rad, and −0.22 rad. In sharp Fano line shapes, a large ER enables low-power operation. The effect of the Q factor on $\Delta\varphi$ is also investigated in Fig. 6(c). Here, $\Delta\varphi$ is defined as the sum of the absolute phase difference between two antisymmetric Fano line shapes ($y_i = |-y_i|$), corresponding to the variation degree of the line shape. The $\Delta\varphi$ tends to increase with Q at $y_i/|-y_i|$ = 4 μm. A larger Q factor means less displacement shift of the input fiber to attain the same $\Delta\varphi$. Although there is much room for improvement in Fano tuning, the impact of the Q factor on the phase tunability of the Fano line shapes is demonstrated for the first time on the LNOI platform. This discovery introduces a new avenue of research for ultra-compact Fano resonance tunability photonic devices.

Conclusion

In this paper, we theoretically proposed and experimentally demonstrated a method for achieving high-Q PCNBCs based on LNOI platform. The design principle of a radiation-limited cavity enabled the successful fabrication of nanocavities with Q factors exceeding 10^5 and high transmittance. To the best of our knowledge, the achieved Q is over one order of magnitude higher than the previous reports on etchless LN PCNBCs. Moreover, we explore the application potential of high Q microcavities in the interaction between light and external fields, demonstrating efficient modulation effects in TO tuning, optically-induced bistability, and Fano line shapes generation. These results hold tremendous promise for providing a versatile platform technique to develop high performance EO or AO modulator, optical logic devices, and quantum photonics, demonstrating significant potential in the field of photonic integration.

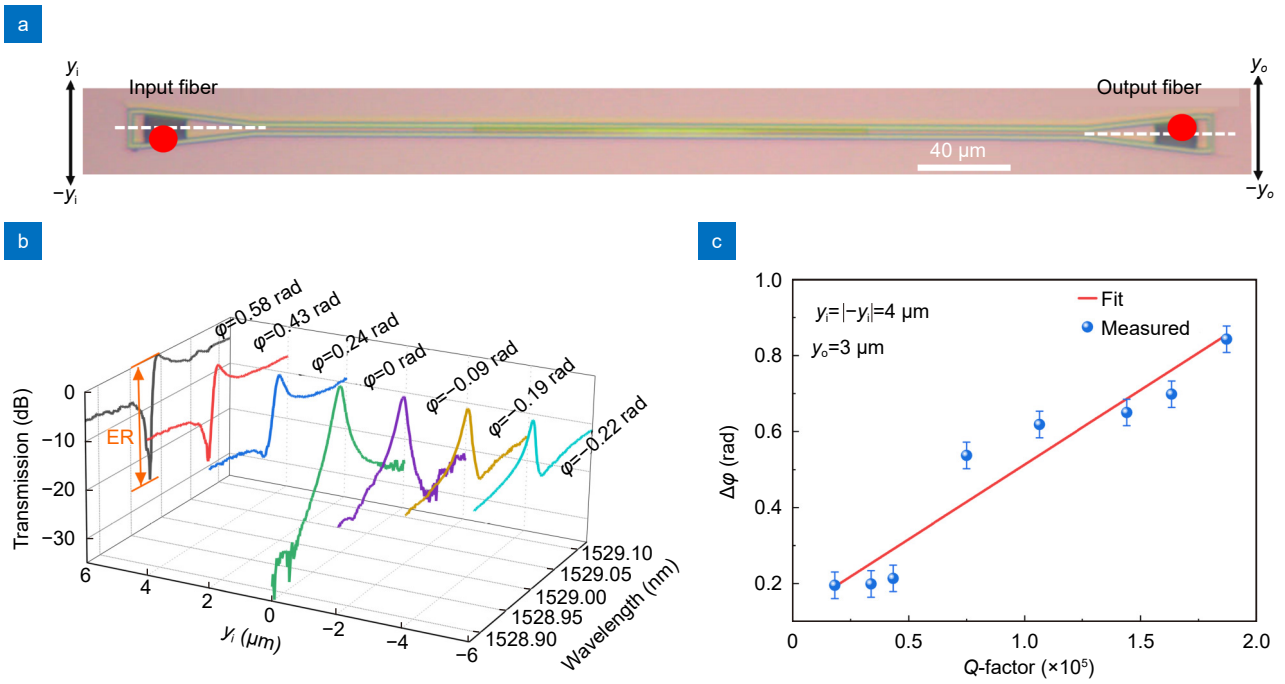

Fig. 6 | (**a**) Optical micrograph of the tested PCNBC. The locations of the fibers are indicated by red dots. (**b**) The measured transmission spectra at different input fiber displacements. The device has a Q of 1.04×10⁵. (**c**) Devices with different Q factors are measured for $\Delta\varphi$.

References

1. Saleh BEA, Teich MC. *Fundamentals of Photonics* 3rd ed (John Wiley & Sons, Hoboken, 2019).
2. Vahala KJ. Optical microcavities. *Nature* **424**, 839–846 (2003).
3. Cocorullo G, Della Corte FG, Rendina I et al. Thermo-optic effect exploitation in silicon microstructures. *Sens Actuators A Phys* **71**, 19–26 (1998).
4. Soref RA, Bennett BR. Electrooptical effects in silicon. *IEEE J Quantum Electron* **23**, 123–129 (1987).
5. Shakoor A, Nozaki K, Kuramochi E et al. Compact 1D-silicon photonic crystal electro-optic modulator operating with ultra-low switching voltage and energy. *Opt Express* **22**, 28623–28634 (2014).
6. Abdollahi Shiramin L, Xie WQ, Snyder B et al. High extinction ratio hybrid graphene-silicon photonic crystal switch. *IEEE Photonics Technol Lett* **30**, 157–160 (2018).
7. Zhang Y, He Y, Zhu QM et al. Single-resonance silicon nanobeam filter with an ultra-high thermo-optic tuning efficiency over a wide continuous tuning range. *Opt Lett* **43**, 4518–4521 (2018).
8. Soljačić M, Joannopoulos JD. Enhancement of nonlinear effects using photonic crystals. *Nat Mater* **3**, 211–219 (2004).
9. Chowdhury MZ, Shahjalal M, Ahmed S et al. 6G wireless communication systems: applications, requirements, technologies, challenges, and research directions. *IEEE Open J Commun Soc* **1**, 957–975 (2020).
10. Zhu D, Shao LB, Yu MJ et al. Integrated photonics on thin-film lithium niobate. *Adv Opt Photonics* **13**, 242–352 (2021).
11. Wooten EL, Kissa KM, Yi-Yan A et al. A review of lithium niobate modulators for fiber-optic communications systems. *IEEE J Sel Top Quantum Electron* **6**, 69–82 (2000).
12. Lam CS. A review of the timing and filtering technologies in smartphones. In *2016 IEEE International Frequency Control Symposium* (*IFCS*) 1–6 (IEEE, 2016); http://doi.org/10.1109/FCS.2016.7546724.
13. Suzuki H, Fujiwara M, Iwatsuki K. Application of super-DWDM technologies to terrestrial terabit transmission systems. *J Lightwave Technol* **24**, 1998–2005 (2006).
14. Wang C, Zhang M, Chen X et al. Integrated lithium niobate electro-optic modulators operating at CMOS-compatible voltages. *Nature* **562**, 101–104 (2018).
15. Li MX, Liang HX, Luo R et al. Photon-level tuning of photonic nanocavities. *Optica* **6**, 860–863 (2019).
16. Cai LT, Mahmoud A, Khan M et al. Acousto-optical modulation of thin film lithium niobate waveguide devices. *Photonics Res* **7**, 1003–1013 (2019).
17. Benchabane S, Robert L, Rauch JY et al. Highly selective electroplated nickel mask for lithium niobate dry etching. *J Appl Phys* **105**, 094109 (2009).
18. Geiss R, Diziain S, Steinert M et al. Photonic crystals in lithium niobate by combining focussed ion beam writing and ion-beam enhanced etching. *Phys Status Solidi A* **211**, 2421–2425 (2014).
19. Wu RB, Zhang JH, Yao N et al. Lithium niobate micro-disk resonators of quality factors above 10^7. *Opt Lett* **43**, 4116–4119 (2018).
20. Gao RH, Zhang HS, Bo F et al. Broadband highly efficient nonlinear optical processes in on-chip integrated lithium niobate microdisk resonators of *Q*-factor above 10^8. *New J Phys* **23**, 123027 (2021).
21. Gao RH, Yao N, Guan JL et al. Lithium niobate microring with ultra-high *Q* factor above 10^8. *Chin Opt Lett* **20**, 011902 (2022).
22. Yu ZJ, Xi X, Ma JW et al. Photonic integrated circuits with bound states in the continuum. *Optica* **6**, 1342–1348 (2019).
23. Zou CL, Cui JM, Sun FW et al. Guiding light through optical bound states in the continuum for ultrahigh-*Q* microresonators. *Laser Photonics Rev* **9**, 114–119 (2015).
24. Yu ZJ, Tong YY, Tsang HK et al. High-dimensional communication on etchless lithium niobate platform with photonic bound states in the continuum. *Nat Commun* **11**, 2602 (2020).
25. Ye F, Yu Y, Xi X et al. Second-harmonic generation in etchless lithium niobate nanophotonic waveguides with bound states in the continuum. *Laser Photonics Rev* **16**, 2100429 (2022).
26. Zhang JX, Pan BC, Liu WX et al. Ultra-compact electro-optic modulator based on etchless lithium niobate photonic crystal nanobeam cavity. *Opt Express* **30**, 20839–20846 (2022).
27. Yu ZJ, Sun XK. Acousto-optic modulation of photonic bound state in the continuum. *Light Sci Appl* **9**, 1 (2020).
28. Yu Y, Yu ZJ, Zhang ZY et al. Wavelength-division multiplexing on an etchless lithium niobate integrated platform. *ACS Photonics* **9**, 3253–3259 (2022).
29. Zhang JH, Ma JY, Parry M et al. Spatially entangled photon pairs from lithium niobate nonlocal metasurfaces. *Sci Adv* **8**, eabq4240 (2022).
30. Valencia Molina L, Camacho Morales R, Zhang JH et al. Enhanced infrared vision by nonlinear up-conversion in nonlocal metasurfaces. *Adv Mater* **36**, 2402777 (2024).
31. Čtyroký J, Petráček J, Kuzmiak V et al. Bound modes in the continuum in integrated photonic $LiNbO_3$ waveguides: are they always beneficial. *Opt Express* **31**, 44–55 (2023).
32. Zhang JX, Liu WX, Pan BC et al. High Q Nanobeam cavity based on etchless lithium niobate integrated platform. In *2021 19th International Conference on Optical Communications and Networks* (*ICOCN*) 1–2 (IEEE, 2021); http://doi.org/10.1109/ICOCN53177.2021.9563667.
33. Quan QM, Loncar M. Deterministic design of wavelength scale, ultra-high Q photonic crystal nanobeam cavities. *Opt Express* **19**, 18529–18542 (2011).
34. Quan QM, Deotare PB, Loncar M. Photonic crystal nanobeam cavity strongly coupled to the feeding waveguide. *Appl Phys Lett* **96**, 203102 (2010).
35. Joannopoulos JD, Johnson SG, Winn JN et al. *Photonic Crystals: Molding the Flow of Light* 2nd ed (Princeton University Press, Princeton, 2008).
36. Li MX, Ling JW, He Y et al. Lithium niobate photonic-crystal electro-optic modulator. *Nat Commun* **11**, 4123 (2020).
37. Zhong H, Zhang RH, He Y et al. Compact photonic crystal nanobeam cavity on Si_3N_4 Loaded LNOI platform. In *2023 Opto-Electronics and Communications Conference* (*OECC*) 1–2 (IEEE, 2023); http://doi.org/10.1109/OECC56963.2023.10209941.
38. Liang HX, Luo R, He Y et al. High-quality lithium niobate photonic crystal nanocavities. *Optica* **4**, 1251–1258 (2017).
39. Witmer JD, Valery JA, Arrangoiz-Arriola P et al. High-*Q* photonic resonators and electro-optic coupling using silicon-on-lithium-niobate. *Sci Rep* **7**, 46313 (2017).
40. Wang J, Shen H, Fan L et al. Reconfigurable radio-frequency arbitrary waveforms synthesized in a silicon photonic chip. *Nat Commun* **6**, 5957 (2015).
41. Stern B, Zhu XL, Chen CP et al. On-chip mode-division multi-

plexing switch. *Optica* **2**, 530–535 (2015).
42. Zhou HY, Qiu CY, Jiang XH et al. Compact, submilliwatt, 2 × 2 silicon thermo-optic switch based on photonic crystal nanobeam cavities. *Photonics Res* **5**, 108–112 (2017).
43. Yu HY, Qiu F. Compact thermo-optic modulator based on a titanium dioxide micro-ring resonator. *Opt Lett* **47**, 2093–2096 (2022).
44. Moretti L, Iodice M, Della Corte FG et al. Temperature dependence of the thermo-optic coefficient of lithium niobate, from 300 to 515 K in the visible and infrared regions. *J Appl Phys* **98**, 036101 (2005).
45. Chen YY, Whitehead J, Ryou A et al. Large thermal tuning of a polymer-embedded silicon nitride nanobeam cavity. *Opt Lett* **44**, 3058–3061 (2019).
46. Quan QM, Burgess IB, Tang SKY et al. High-Q, low index-contrast polymeric photonic crystal nanobeam cavities. *Opt Express* **19**, 22191–22197 (2011).
47. Yao DY, Jiang Z, Zhang Y et al. Ultrahigh thermal-efficient all-optical silicon photonic crystal nanobeam cavity modulator with TPA-induced thermo-optic effect. *Opt Lett* **48**, 2325–2328 (2023).
48. Liu XY, Ying P, Zhong XM et al. Highly efficient thermo-optic tunable micro-ring resonator based on an LNOI platform. *Opt Lett* **45**, 6318–6321 (2020).
49. Li GL, Zheng XZ, Yao J et al. 25Gb/s 1V-driving CMOS ring modulator with integrated thermal tuning. *Opt Express* **19**, 20435–20443 (2011).
50. Gao Y, Zhou W, Sun XK et al. Cavity-enhanced thermo-optic bistability and hysteresis in a graphene-on-Si_3N_4 ring resonator. *Opt Lett* **42**, 1950–1953 (2017).
51. Almeida VR, Lipson M. Optical bistability on a silicon chip. *Opt Lett* **29**, 2387–2389 (2004).
52. Wen PY, Sanchez M, Gross M et al. Vertical-cavity optical AND gate. *Opt Commun* **219**, 383–387 (2003).
53. Thierfelder C, Sanna S, Schindlmayr A et al. Do we know the band gap of lithium niobate. *Phys Status Solidi C* **7**, 362–365 (2010).
54. Barclay PE, Srinivasan K, Painter O. Nonlinear response of silicon photonic crystal microresonators excited via an integrated waveguide and fiber taper. *Opt Express* **13**, 801–820 (2005).
55. Nozaki K, Shinya A, Matsuo S et al. Ultralow-energy and high-contrast all-optical switch involving Fano resonance based on coupled photonic crystal nanocavities. *Opt Express* **21**, 11877–11888 (2013).
56. Su JY, Huang XQ, Xu HL et al. Ultrafast all-optical switching in a silicon-polymer compound slotted photonic crystal nanobeam cavity. *Opt Rev* **30**, 33–40 (2023).
57. Zheng S, Ruan ZS, Gao SQ et al. Compact tunable electromagnetically induced transparency and Fano resonance on silicon platform. *Opt Express* **25**, 25655–25662 (2017).
58. Guo XQ, Dai TG, Chen B et al. Twin-Fano resonator with widely tunable slope for ultra-high-resolution wavelength monitor. *Opt Lett* **44**, 4527–4530 (2019).
59. Mehta KK, Orcutt JS, Ram RJ. Fano line shapes in transmission spectra of silicon photonic crystal resonators. *Appl Phys Lett* **102**, 081109 (2013).
60. Gu LP, Wang BB, Yuan QC et al. Fano resonance from a one-dimensional topological photonic crystal. *APL Photonics* **6**, 086105 (2021).
61. Galli M, Portalupi SL, Belotti M et al. Light scattering and Fano resonances in high-Q photonic crystal nanocavities. *Appl Phys Lett* **94**, 071101 (2009).
62. Limonov MF, Rybin MV, Poddubny AN et al. Fano resonances in photonics. *Nat Photonics* **11**, 543–554 (2017).

Acknowledgements

We are grateful for financial supports from the National Key R&D Program of China (No. 2022ZD0119002), the National Natural Science Foundation of China (Grant No. 62025402, 62090033, 92364204, 92264202 and 62293522) and Major Program of Zhejiang Natural Science Foundation (Grant No. LDT23F04024F04)

Author contributions

Z. Jiang and C. Z. Fang designed the devices and wrote the original manuscript. X. Ran, Y. Gao and R. Q. Wang performed the simulations and experimental characterization. J. G. Wang fabricated the samples. D. Y. Yao and X. T. Gan proposed the original idea. Y. Liu supervised the project. All authors reviewed and revised the manuscript with valuable suggestions.

Competing interests

The authors declare no competing financial interests.